Received: 20 August 2021 | Revised: 26 June 2022 | Accepted: 1 July 2022

DOI: 10.1002/nag.3427

RESEARCH ARTICLE

WILEY

Development and validation of a computationally efficient hybrid model for temporal high-resolution simulations of geothermal bore fields

Stephan Düber[1,2] | **Martin Ziegler**[3] | **Raul Fuentes**[1]

[1]Institute of Geomechanics and Underground Technology, RWTH Aachen University, Aachen, Germany

[2]Department of Infrastructure Engineering, The University of Melbourne, Parkville, Australia

[3]Ziegler und Aulbach Ingenieurgesellschaft mbH, Managing Director, Professor (Emeritus), Ziegler und Aulbach Ingenieurgesellschaft mbH, Aschaffenburg, Germany

Correspondence
Stephan Düber, Institute of Geomechanics and Underground Technology, RWTH Aachen University, Aachen, Germany.
Email: dueber@gut.rwth-aachen.de

Abstract

This paper presents a hybrid simulation approach for 1U-, 2U- and coaxial single, and field of, borehole heat exchangers. We implement a novel combination of existing solutions for the simulation of heat transfer processes within the borehole and the surrounding ground. The heat transfer in the ground is modelled with a combination of analytically determined g-functions, the borehole models utilize thermal resistance capacity models and the finite volume method. Critically, we improve the computational efficiency of long-term simulations by sub-dividing the time scale into multiple periods, where the influence of past periods on future periods is calculated using the fast Fourier transform (FFT). The accuracy and efficiency of the proposed method is validated against single borehole numerical models and a 40 bore field case study. The method achieves computational times reductions of over 90% in some cases, with greater improvement as the simulation time increases.

KEYWORDS

borehole heat exchanger, fast Fourier transform, g-function, Python, thermal resistance capacitance

1 | INTRODUCTION

The design and simulation of geothermal systems with borehole heat exchangers can be challenging due to the three-dimensional heat transfer processes in the ground and the heat exchanger, the large spatial scale differences and the long operational periods. The scale-distributed geometries and transient transfer processes lead to high computational costs when using numerical models. For example, traditional design periods of 50 years mean that, such models are not often used in practice.[1] Simplified solutions with some limitations are widely preferred due to their simpler handling and short computational times. In most common solutions, the spatial domain is divided into two parts, the domain inside the borehole and the domain outside the borehole (see Figure 1, left). One advantage of this approach is that different simulation methods can be used for both areas.

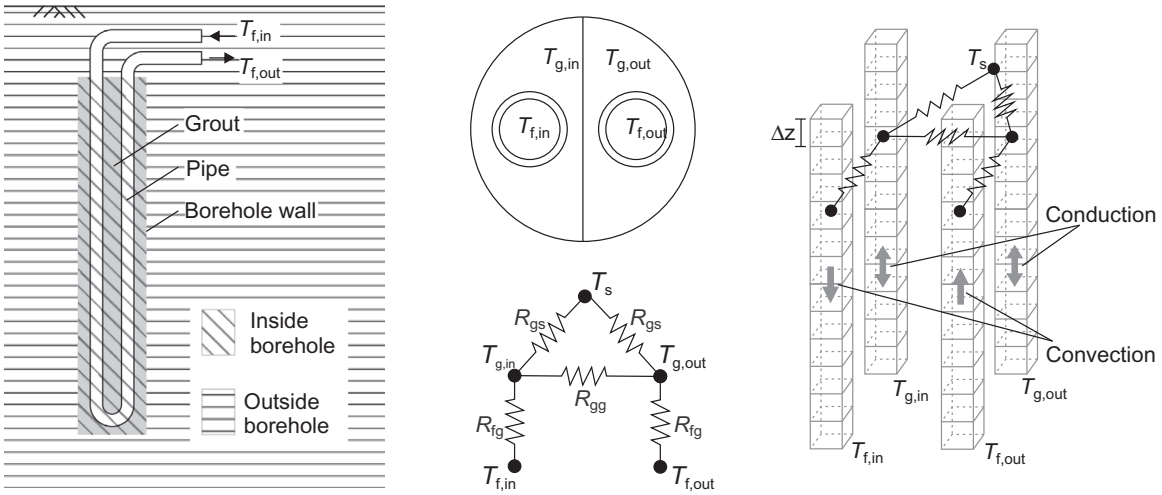

FIGURE 1 Schematic illustrations of a 1U-BHE model: longitudinal section (left); cross section and resistance model with temperature nodes (middle); vertical discretisation and transfer processes, the resistances and temperature nodes are shown exemplary for one horizontal plane (right)

A computationally efficient method for the area outside the borehole is the g-function approach introduced by Eskilson.[2] G-functions are thermal response functions that can be used to calculate the temperature response at the borehole wall or any other point in the ground for an imposed constant load. For time-varying loads, as they occur in reality, Duhamel's theorem, from now on referred to as superposition principle, is typically applied.[3] To speed up computational time for high-resolution time variable loads, Marcotte and Pasquier[4] proposed to solve the problem in the Fourier domain using the convolution theorem.

G-functions depend on the borehole geometry and the characteristic time[2] $t_s = H^2/9\alpha_s$ where H is the length of the borehole and α_s the thermal diffusivity of the ground and can be derived with numerical or analytical methods. While Eskilson[2] and others[5] determine g-functions numerically, a variety of analytical solutions exist. One key element is the geometry used to model the borehole in a simplified way. While the infinite line source (ILS) considers the borehole as an infinite one-dimensional heat source in infinite space,[3,6] the finite line source (FLS) considers the finite length of the borehole in semi-infinite space.[7] In contrast to line sources models, cylinder source models consider the actual radius of the borehole.[3,8–10] Philippe et al.[11] show the different validity ranges in the time domain of the mentioned solutions. While the FLS provides better results for short boreholes or long observation periods, the cylinder source models lead to more accurate results for short-term observations because of the relative importance of the borehole geometry initially in the short-term. Li et al.[12] combine the different models and derive a g-function that produces accurate results over the entire time scale and call it *fullscale* g-function.

To account for groundwater flow in homogeneous soil, the borehole can be modelled as a moving line[3,13,14] or cylinder sources.[15] Other extensions of the FLS consider inhomogeneous soil structure[16] and horizontal groundwater flow through sequences of permeable and impermeable soil layers.[17]

By dividing the borehole into multiple segments, Cimmino and Bernier[18] developed a method based on the FLS for determining the g-function of BHE fields with different boundary conditions, such as equal borehole wall temperature in all boreholes.

While the approaches mentioned above are used to calculate temperatures outside and at the borehole wall, others also include the heat exchanger itself[5,19–23]

An alternative method to cover the processes inside the borehole are models based on thermal resistances and capacities.[24–30] In this approach, the horizontal heat flows are modelled with a circuit of coupled thermal resistances (see Figure 1, middle). The convective heat flows in the circulating fluid can be solved analytically with a few simplifications by coupled partial differential equations[31] or numerical methods.[32,33] Models that use thermal resistance capacitance models (TRCM) for the horizontal heat transfer and numerical methods for the vertical heat transfer within the fluid are referred to as numerical borehole models here on. Combining both approaches explained above, various simulation tools use a combination of numerical borehole models and g-functions. The simulation tool *EWS* couples a TRCM with numerical or analytical derived g-functions.[34] Ruiz-Calvo et al.[35] include the near ground effects in the numerical BHE model and

couple it with a g-function for the far-field and a load aggregation scheme. The model presented by Düber[36] combines TRCM with a fullscale analytical g-function. Laferrière et al.[37] also use a fullscale analytical g-function coupled to a TRCM and combine it with a load aggregation scheme. All of the above report accurate results against different conditions. However, their efficiency in terms of computational time when not using a load aggregation scheme could be improved. This is of particular importance when the number of boreholes in a field is large or when the modelled times are long, as in the real-life operation of such systems, e.g. 100 years or longer.

This paper presents an extension to the model from Düber,[36] incorporating the application of the fast Fourier transformation to perform high temporal resolution simulations of multiple BHE in a computationally efficient manner. By using this method, the calculation time could be reduced significantly without the use of a load aggregation scheme. The paper starts with a description of the model in Section 2, followed by a validation and demonstration in Section 3 using single borehole with 1U-, 2U- and coaxial type heat exchangers, and a borehole field consisting of 40 2U-BHEs. Finally, a discussion and conclusions are presented. All models are implemented in Python and are available through a GitHub repository.[38]

2 | MODEL

2.1 | Model structure and simulation process

The presented model has several components: the simulation methods for the domains inside and outside the borehole; the coupling of the two and; the integration of the FFT model for the domain outside the borehole. Furthermore, a method for the determination of model specific parameters is presented to demonstrate its use.

2.1.1 | Heat transfer inside the borehole

Here we use the implementation of Bauer et al.[27] for the thermal resistances and the spatial division of the grout material for 1U-, 2U- and Coaxial-BHE with an annular inlet.

The heat transfer in the vertical direction is a combination of heat conduction in the grout material and convection in the fluid and is governed by the transient convection-diffusion equation

$$\varrho c \frac{\partial T}{\partial t} = \boldsymbol{\nabla} \cdot (\lambda \boldsymbol{\nabla} T - \upsilon \varrho c T) + q_{\mathrm{h}} \tag{1}$$

which is discretised using the finite volume method. In Equation (1) T denotes the temperature, t the time, ϱc the volumetric heat capacity, λ he thermal conductivity, υ the fluid velocity and q_{h} the source term. As shown in Figure 1 on the right, the equation is discretised and solved in 1D for each temperature node within the borehole. For the grout material this results in

$$\varrho c \frac{\partial T}{\partial t} = \boldsymbol{\nabla} \cdot (\lambda \boldsymbol{\nabla} T) + q_{\mathrm{h}} \tag{2}$$

and for the temperatures in the fluid, neglecting conduction

$$\varrho c \frac{\partial T}{\partial t} = \boldsymbol{\nabla} \cdot (-\upsilon \varrho c T) + q_{\mathrm{h}}. \tag{3}$$

Different numerical interpolation schemes are used for Equations (2) and (3). The diffusion term (Equation 2) is interpolated with the central difference scheme (CDS) whereas the convective term (Equation 3) is approximated with the upwind scheme to prevent oscillating solutions for high Péclet numbers. Besides being computationally efficient, the upwind scheme does not produce any non-physical solutions (e.g. oscillations), which may produce problems when coupling the model with other system component models. On the other hand, the upwind scheme can introduce numerical diffusion, which can be controlled by adequate spatial and time discretisation, depending on the numerical integration method.

The heat transfer in the horizontal direction is solved with analytical equations based on Fourier's law. The horizontal heat flows q_{h} are integrated as a source term in Equation (1), and they depend on the total thermal resistance R_{th} (e.g. the

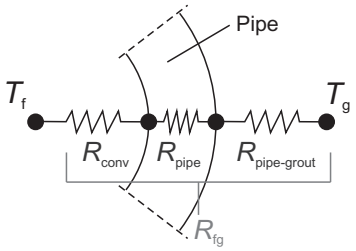

FIGURE 2 Exemplary illustration of the elements of the thermal resistance between fluid and grout

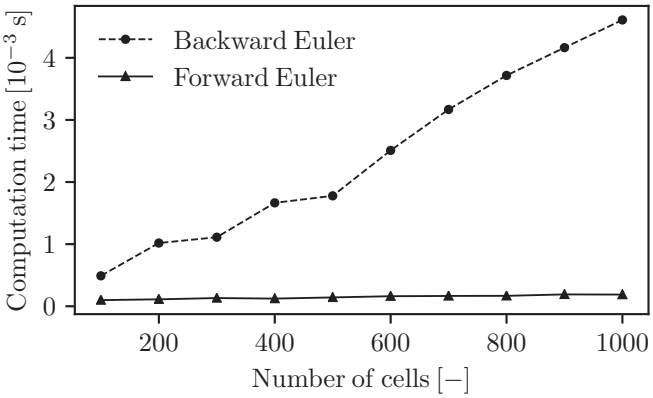

FIGURE 3 Computational time per step for forward and backward Euler BHE models depending on vertical discretization. Processing unit is an Intel i7-7700K processor at 4200 MHz, 16 GB of RAM, Windows version 10

resistance between fluid and grout R_{fg}, or the resistance between grout and soil R_{gs}), the cell height Δz and are driven by the temperature gradient ΔT between two temperature nodes (e.g. $T_{f,in} - T_{g,in}$ or $T_{g,in} - T_s$, as shown in the nodes-resistance model in Figure 1):

$$q_h = \frac{\Delta z \cdot \Delta T}{R_{th}}. \tag{4}$$

The total thermal resistances R_{th} are serial connections of convective and diffusive resistances. For example, the resistance between the fluid and the grout is a serial connection of the convective resistance between the fluid and the inner wall of the pipe R_{conv}, the conductive resistance of the pipe R_{pipe} and the conductive resistance between the outer wall of the pipe and the thermal centre of the grout $R_{pipe-grout}$ (Figure 2). While the conductive resistances are calculated based on the geometry and thermal properties of the material, the convective resistance is based on the dimensionless flow coefficients *Reynolds*, *Nusselt* and *Prandtl*. Detailed compilations of all equations are given in Diersch et al.[39] and Bauer et al.[27]

For the numerical integration of Equation (1), the forward and backward Euler methods are implemented and compared. The Euler method was chosen for its simplicity and efficiency. Depending on fluid velocity, spatial and temporal discretization or desired accuracy, one of the methods may be advantageous over the other. While the backward scheme is preferred in general due to its robustness and unconditional stability, the forward scheme can be more computationally efficient for certain conditions. It is also easier to reduce the numerical diffusion caused by the upwind method in the forward scheme by choosing a Courant–Friedrichs–Lewy (CFL) number close to 1, while for the backward method the spatial and temporal discretisation have to be refined. Figure 3 shows the computational time per timestep for the 2U-BHE model. The computational times of the BHE models are driven only by the number of cells, as no internal iteration is required for the forward models and a direct solver (*scipy.sparse.linalg.spsolve*[40]) is used for the backward models. For a model with 100 cells for each temperature node, the Forward Euler implementation is about five times faster than the backward Euler model. With increasing number of cells, the difference between the two schemes also increases linearly. Despite these results, it cannot be concluded that the forward scheme will always be the best choice in terms of computational effort as it depends on the timestep. The maximum timestep that can be used depends on cell size and fluid velocity,

according to Fichter,[41] it can be calculated using the CFL condition as

$$\Delta t_{\max} = \left(\frac{\upsilon}{\Delta z} + \frac{2\alpha}{(\Delta z)^2} + \sum_i \frac{\Delta z}{\varrho c R_{\text{th}} \Delta V} \right)^{-1}. \tag{5}$$

The first term of Equation (5) accounts for the convection, the second term with the thermal diffusivity α for conduction in vertical direction and the last term with the cell volume ΔV for the horizontal heat transfer. The total thermal resistance R_{th} is calculated according to the pipe configuration[27,39] and the cell type. To obtain the overall maximum timestep size for the forward implementation, Equation (5) has to be solved for the grout and the fluid cells. Accordingly, the following results for a 1U-BHE configuration as shown in Figure 1 with the thermal resistances between fluid and grout R_{fg}, between the two grout sections R_{gg} and between grout and soil R_{gs}:

$$\Delta t_{\max,\text{fluid}} = \left(\frac{\upsilon}{\Delta z} + \frac{\Delta z}{\varrho c_{\text{f}} R_{\text{fg}} \Delta V} \right)^{-1} \tag{6}$$

and

$$\Delta t_{\max,\text{grout}} = \left(\frac{2\alpha}{(\Delta z)^2} + \frac{\Delta z}{\varrho c_{\text{g}} R_{\text{fg}} \Delta V} + \frac{\Delta z}{\varrho c_{\text{g}} R_{\text{gg}} \Delta V} + \frac{\Delta z}{\varrho c_{\text{g}} R_{\text{gs}} \Delta V} \right)^{-1}. \tag{7}$$

The minimum of $\Delta t_{\max,\text{fluid}}$ and $\Delta t_{\max,\text{grout}}$ is the decisive timestep for the simulation.

2.1.2 | Heat transfer outside the borehole

For the domain outside the borehole, the g-function approach introduced by Eskilson[2] is used. The temperature at the borehole wall T_{b} due to an imposed load q is calculated as follows:

$$T_{\text{b}} = T_0 + \frac{q}{2\pi\lambda_{\text{s}}} \cdot g\left(\frac{t}{t_{\text{s}}}, \frac{r_{\text{b}}}{H}, \frac{D}{H} \right). \tag{8}$$

The second term of Equation (8) represents the temperature change due to the imposed load, where T_0 is the undisturbed ground temperature. Here λ_{s} denotes the thermal conductivity of the soil, r_{b} the borehole radius and D the buried depth.

Three of the main analytical solutions to calculate g to date are the infinite cylinder source (ICS),[10] the FLS[7] and the ILS.[3] As shown by Philippe et al.,[11] the ICS works most accurately for the shortest dimensionless time, whereas the ILS is only accurate for the medium term and the FLS for the longer term. Inspired by the work of Li et al.,[12] we use a combination of different analytical derived g-functions to cover the full-time range[36,37]:

$$g_{\text{fullscale}} = g_{\text{ICS}} + g_{\text{FLS}} - g_{\text{ILS}}. \tag{9}$$

While for the short- and medium-term ILS and FLS overlap, the same is true for the medium and long terms for ICS and ILS. This allows us to intersect the different approaches according to Equation (9) and thus calculate a combined *fullscale* g-function that is valid for the entire time range. We use the FLS formulation proposed by Claesson and Javed[21] to calculate the integral mean temperature along the borehole. For the ICS, we favour the easy to evaluate formulation proposed by Man et al.[10].

For multiple boreholes, the spatial superposition principle[3] can be used to account for thermal interaction:

$$\Delta T_{\text{b},i} = \sum_{j=1}^{n_{\text{b}}} \frac{q_j}{2\pi\lambda_{\text{s}}} g_j(d_{ji}) \tag{10}$$

$$d_{ji} = \begin{cases} r_{\text{b},i} & \text{for } i = j \\ \sqrt{(x_i - x_j)^2 + (y_i - y_j)^2} & \text{for } i \neq j \end{cases} \tag{11}$$

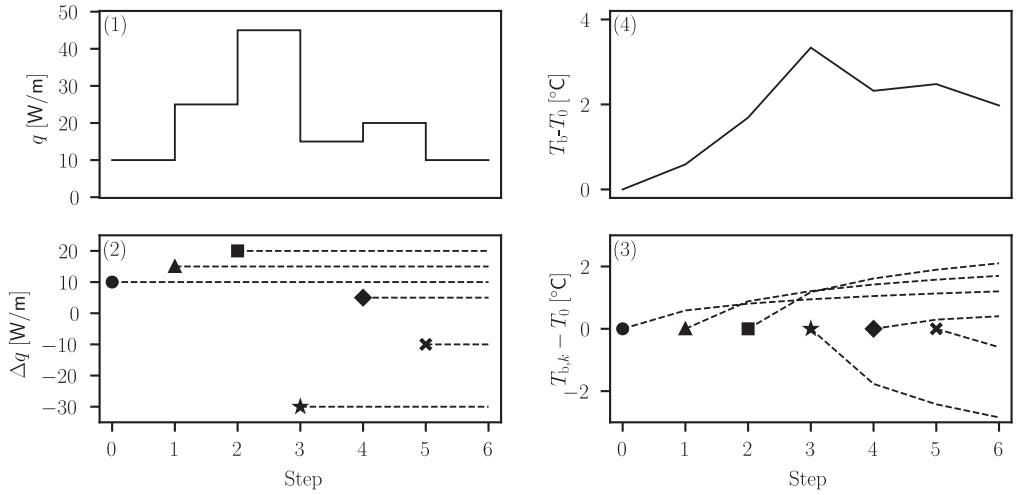

FIGURE 4 Application of the superposition principle for time-varying loads: decomposition of the load (1) as load increments (2) and superposition of the temperature responses (3) to construct the solution (4). After Marcotte and Pasquier[4] and Lazzarotto[42]

This means the temperature change ΔT_b at the borehole i is the sum of the temperature changes due to all considered boreholes with coordinates (x_j, y_j) and their associated loads q_j. For the consideration of time variable loads, temporal superposition can be applied where $q(t)$ (Figure 4, (1)) is divided into load increments $\Delta q(t_k) = q(t_k) - q(t_{k-1})$ (Figure 4, (2)). The temperature change at any step k (Figure 4, (4)) is the sum of all past temperature responses (Figure 4, (3)) at their respective load increments. Including the summation over time into Equation (10) leads to

$$\Delta T_{b,i,k} = \sum_{l=1}^{k} \sum_{j=1}^{n_b} \frac{\Delta q_{j,l}}{2\pi\lambda_s} g_{j,k-l+1}(d_{ji}). \tag{12}$$

2.1.3 | Coupling of borehole and underground model

The coupling parameter between the numerical borehole model and the g-function model is the soil temperature at the borehole wall T_b. Based on the soil temperature and the fluid inlet temperature, the borehole model calculates new temperatures for all BHE components. The difference between the mean grout temperature $\overline{T}_g$ and the soil temperature T_b and the thermal resistance between grout and soil R_{gs} determine the ground load:

$$q = \frac{T_b - \overline{T}_g}{R_{gs}}. \tag{13}$$

The ground load serves as input for the g-function model to calculate the soil temperature at the borehole wall. As the borehole wall temperature depends on the grout temperature, which also depends on the borehole wall temperature, this problem requires an iterative scheme as shown in Figure 5. As a first guess of the soil temperature, we use the value at the previous timestep $i - 1$. After calculating a new ground temperature, this process is repeated, until an error tolerance criterion is fulfilled. The deviation of the outlet fluid temperature between two iterations is used as error criterion:

$$e = \left| \frac{T_{f,out}^{new} - T_{f,out}^{old}}{T_{f,out}^{old}} \right|. \tag{14}$$

The error tolerance has a negligible influence as long as sufficient iterations are allowed. After the error criterion is met, the g-function model is used to calculate the temperature change according to the ground load increment $\Delta q(t_k) = q(t_k) - q(t_{k-1})$ for all future timesteps.

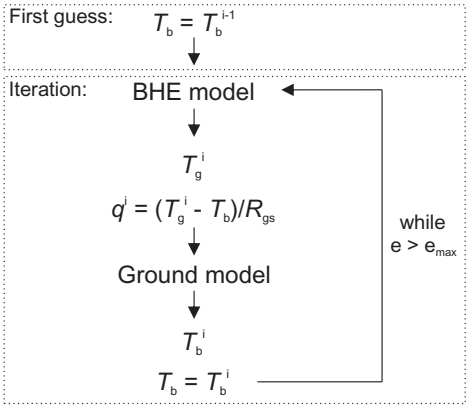

FIGURE 5 Scheme of the coupling process between borehole and ground model

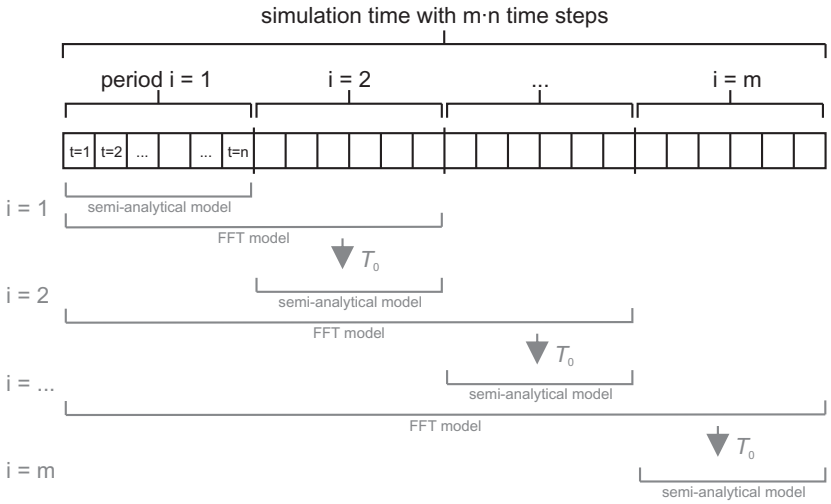

FIGURE 6 Simulation setup with periods (black) and simulation process (grey)

2.1.4 | Integration of fast Fourier transform

A disadvantage of the previously presented model, from now on referred to as *semi-analytical model*, is that the computational time increases exponentially with increasing simulation steps as the ground temperatures have to be calculated for all future timesteps in each timestep. For example, in the case shown in Figure 4, the temperatures due to the first load increment (marked with a circle) must be calculated for timesteps 1–6. For the second increment (marked with a triangle) for steps 2–6 and so on. However, Marcotte and Pasquier[4] have shown that the computation of the ground temperature can be seen as a convolution in the time domain that can be efficiently evaluated by using the fast Fourier transform (FFT). Applying the FFT to Equation (12) leads to

$$\Delta T_{b,i} = \sum_{j=1}^{n_b} \mathcal{F}^{-1}\left(\mathcal{F}\left(\frac{\Delta q_j}{2\pi\lambda_s}\right) * \mathcal{F}(g_j(d_{ji}))\right) \tag{15}$$

where $\mathcal{F}$ is the direct and $\mathcal{F}^{-1}$ the inverse FFT. Here we use the *scipy.fft* module[40] to calculate $\mathcal{F}$ and $\mathcal{F}^{-1}$.

Replacing Equation (12) by Equation (15) can reduce the computational time by several orders of magnitude, depending on the number of timesteps. To make use of Equation (15), the load increments Δq for all timesteps have to be known, which means it cannot be used directly in the semi-analytical model. However, if we divide the simulation time into multiple time periods (see Figure 6) and use the FFT, each of these periods can be simulated using the semi-analytical model. After a period is simulated, all load increments of this period are passed to a second model, from now on referred to as *FFT model*, which uses Equation (15) to calculate the ground temperatures for the following period. These temperatures become the initial temperatures T_0 for the next period.

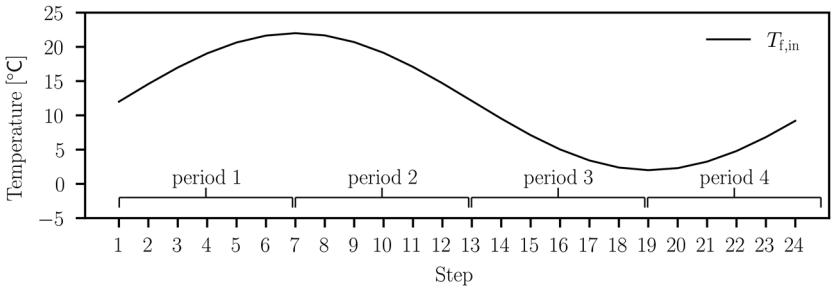

FIGURE 7 Inlet temperature and simulation setup for an exemplary simulation

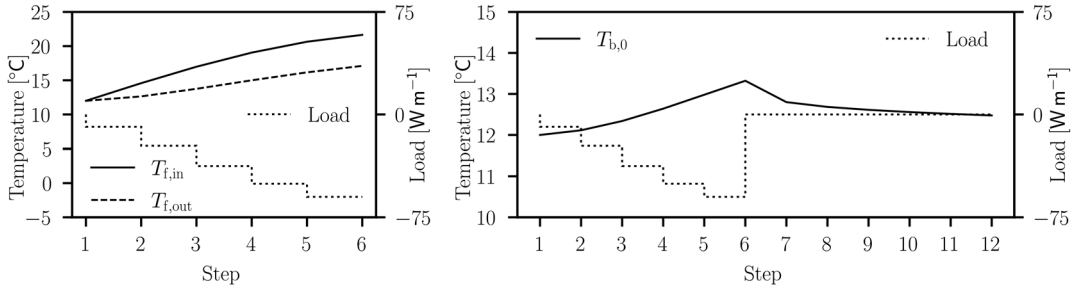

FIGURE 8 Results of the semi-analytical model (left) and the FFT model (right) for the first iteration i according to Figure 6

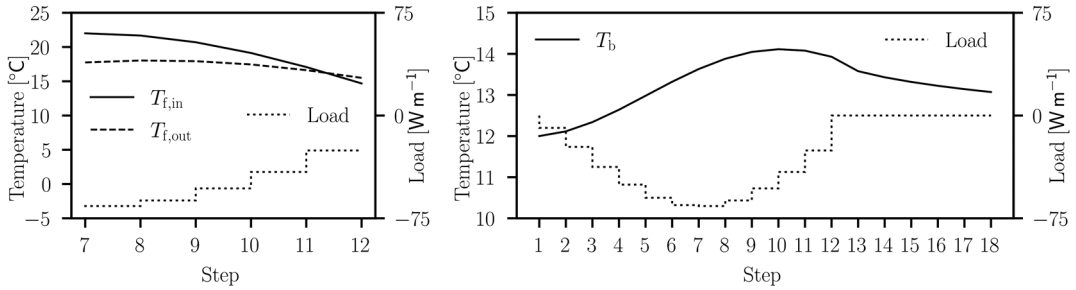

FIGURE 9 Results of the semi-analytical model (left) and the FFT model (right) for the second iteration i according to Figure 6

To give a more practical example, let us assume a simulation with 26 time steps with a known inlet temperature as boundary condition. The simulation time is divided into four periods with six time steps each (Figure 7). The undisturbed ground temperature is 12°C. With the undisturbed ground temperature and the fluid inlet temperature, the semi-analytical model is used to simulate the first period. Results of the simulation are, among others, the outlet fluid temperature and the corresponding ground load (Figure 8, left). This ground load is now passed to the FFT model. According to the number of time steps of the next period, zeros are appended to the load vector. With this load vector (Figure 8, right), the FFT model calculates the ground temperature at the borehole wall for the time steps of the first two periods (Figure 8, right). The temperatures for the first period are a by-product and already known from the simulation with the semi-analytical model, while the temperatures for the second period serve as inputs for the simulation of the second period with the semi-analytical model. While for the simulation of the first period with the semi-analytical model, the undisturbed ground temperature was initialized with 12°C, it is now set to the values calculated by the FFT model for the time steps of the second period as shown in Figure 8 on the right.

Finally, this procedure is repeated for all further periods. The semi-analytical model is used to determine the outlet temperature and the load for the second period (Figure 9, left). Using the loads from the first two periods, the FFT model is used again to calculate the ground temperatures for simulation of the third period with the semi-analytical model (Figure 9, left). The procedure is repeated until all periods are calculated (Figure 10). The simulation of the last period with the semi-analytical model is not shown here, but Figure 11 shows the overall result of the simulation.

In the semi-analytical model, the g-function model has to be solved at each timestep for all following timesteps of the period (Equation 12). The FFT model, however, needs to be computed only once for each period, as the temperature responses for all timesteps are obtained simultaneously by solving Equation (15). This procedure reduces the effect of the

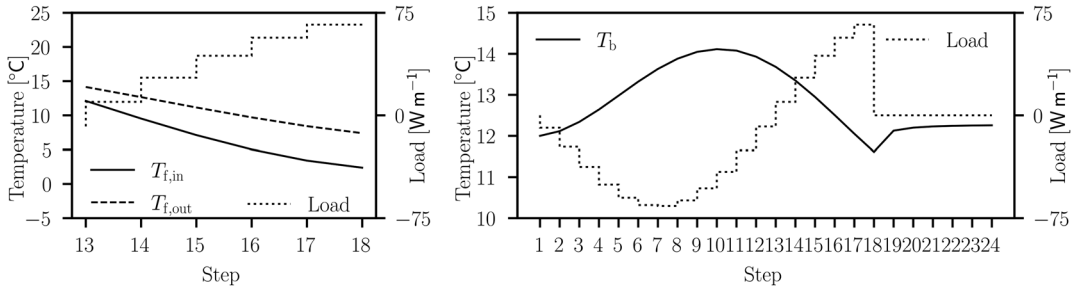

FIGURE 10 Results of the semi-analytical model (left) and the FFT model (right) for the third iteration i according to Figure 6

FIGURE 11 Final result of the exemplary simulation

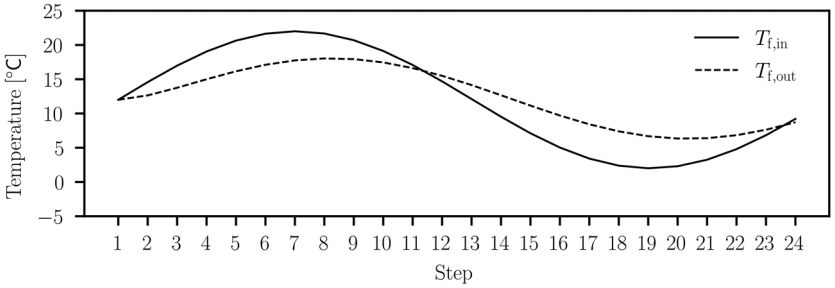

exponential growth of the computational time as a function of the timesteps. For example, if the computational time is defined as $\Delta t = \psi n_s^2$ where n_s is the number of timesteps for the full modelling time, this leads to a computational time of $\Delta t = \psi 100^2$. With the sub-division in periods and FFT, the time becomes $\Delta t = 10 \cdot \psi 10^2$, which is 10 times shorter. Both the computational time of the semi-analytical model and the FFT model depend on the number of timesteps per period. This analysis aims to determine the optimal number of periods depending on the total number of timesteps.

2.2 | Division of the simulation time

The procedure shown in Figure 6 leads to the question though of how many periods the simulation time must be divided into for the most efficient simulation, which we solve in this section. To provide a more application-oriented view and include memory access times, it was decided to base the analysis on measured process times.

Considering one period with the semi-analytical model, the computational time for the temperature response of each load increment decreases with progressing simulation time, as the temperature response has to be calculated only for the remaining timesteps n_r.

Due to the linear time complexity of the operations involved, the computational time for a timestep Δt_{step} can then be defined, in general, as a linear function of the remaining timesteps n_r times a constant factor ψ_{sa} as follows plus a constant c_{sa} that accounts for setup and memory access time:

$$\Delta t_{step} = \psi_{sa} n_r + c_{sa}. \tag{16}$$

This becomes clear when determining ψ_{sa} by measuring the computational time for different n_r as shown in Figure 12. The line has two sections separated at a breakpoint of $n_{bp} = 130,000$. This breakpoint occurs because of the way the data are handled within the PC. Their location will change depending on the data types, operating system, compilers and so forth. Hence, it needs to be calculated for each hardware and software set-up individually. The same applies to the other parameters derived from measured computational times. Since the calculation is only an array multiplication and subtraction, the only relevant parameter is the number of elements n_r. The linear fit leads to

$$\psi_{sa} = \begin{cases} 5.8 \times 10^{-10} & \text{for } n_r < 130,000 \\ 3.7 \times 10^{-9} & \text{for } n_r \geq 130,000 \end{cases} \tag{17}$$

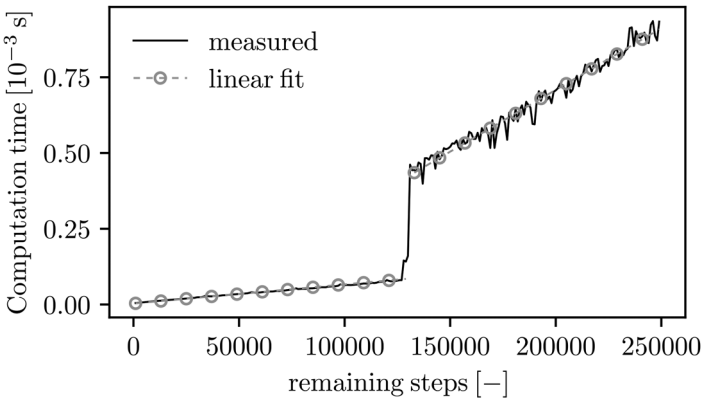

FIGURE 12 Computational time per timestep of the ground model in the semi-analytical model depending on the number of remaining steps. The calculation consists of multiplying the load increment by the g-function for the remaining time steps, and adding the calculated temperature change to the previous temperature

and

$$c_{\mathrm{sa}} = \begin{cases} 5.4 \times 10^{-6} & \text{for } n_{\mathrm{r}} < 130,000 \\ -9.1 \times 10^{-5} & \text{for } n_{\mathrm{r}} \geq 130,000 \end{cases} \tag{18}$$

These values depend on the computer used, the operating system and other factors and are not generally valid. A script for determining the values for any other setup is included in the repository.[38]

The fitted line though allows predicting the total computational time of the entire period Δt_{per}, which is defined as a function of the number of steps per period n_{sp}:

$$\Delta t_{\mathrm{per}} = \sum_{i=0}^{n_{\mathrm{sp}}-1} \psi_{\mathrm{sa}}(n_{\mathrm{sp}} - i) + c_{\mathrm{sa}} = \frac{\psi_{\mathrm{sa}}}{2}({n_{\mathrm{sp}}}^2 + n_{\mathrm{sp}}) + c_{\mathrm{sa}} n_{\mathrm{sp}}. \tag{19}$$

When resolving the summation in Equation (19), it should be noted that different values of ψ_{sa} and c_{sa} apply depending on the side of the breakpoint at which the function is evaluated. When n_{sp} is bigger than n_{bp}, new values $\bar{\psi}_{\mathrm{sa}}$ and $\bar{c}_{\mathrm{sa}}$ are necessary. By introducing $\psi_{\mathrm{sa}} = \psi_{\mathrm{sa}}^{<}$ for $n_{\mathrm{r}} < n_{\mathrm{bp}}$ and $\psi_{\mathrm{sa}} = \psi_{\mathrm{sa}}^{>}$ for $n_{\mathrm{r}} \geq n_{\mathrm{bp}}$ and applying the same for c_{sa}, we can calculate weighted parameters (see Appendix B for more details on $\bar{\psi}_{\mathrm{sa}}$):

$$\bar{\psi}_{\mathrm{sa}} = \frac{n_{\mathrm{bp}}^2(\psi_{\mathrm{sa}}^{<} - \psi_{\mathrm{sa}}^{>}) + n_{\mathrm{bp}}(\psi_{\mathrm{sa}}^{>} - \psi_{\mathrm{sa}}^{<}) + \psi_{\mathrm{sa}}^{>}(n_{\mathrm{sp}}^2 + n_{\mathrm{sp}})}{n_{\mathrm{sp}}^2 - n_{\mathrm{sp}}} \tag{20}$$

$$\bar{c}_{\mathrm{sa}} = \frac{n_{\mathrm{sp}} - (n_{\mathrm{bp}} - 1)}{n_{\mathrm{sp}}} c_{\mathrm{sa}}^{>} + \frac{n_{\mathrm{bp}} - 1}{n_{\mathrm{sp}}} c_{\mathrm{sa}}^{<} \tag{21}$$

However, the implementation of the FFT has a linearithmic time complexity, which is linearly approximated for simplicity. This will lead to a negative ordinate intersection for an unconstrained linear fit. Since this does not correspond to reality, and also leads to problems in the following calculations, we will constrain the ordinate intersection to zero for the linear approximation, so that the relation between the computational time and the number of steps n for the FFT model can be defined as

$$\Delta t = \psi_{\mathrm{FFT}} n. \tag{22}$$

Figure 13 shows the computational time of the FFT model depending on the number of steps measured with the model. The linear approximation leads to $\psi_{\mathrm{FFT}} = 1.58 \times 10^{-6}$.

The total computational time for the FFT model for all periods is

$$\Delta t_{\mathrm{FFT}} = \sum_{i=1}^{n_{\mathrm{per}}-1} (i+1) n_{\mathrm{sp}} \psi_{\mathrm{FFT}} = \frac{\psi_{\mathrm{FFT}}}{2} n_{\mathrm{sp}}({n_{\mathrm{per}}}^2 + n_{\mathrm{per}} - 2), \tag{23}$$

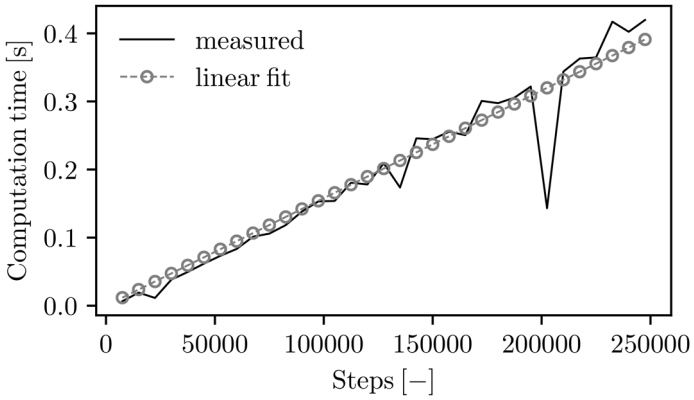

FIGURE 13 Computational time of the FFT model depending on the number of steps

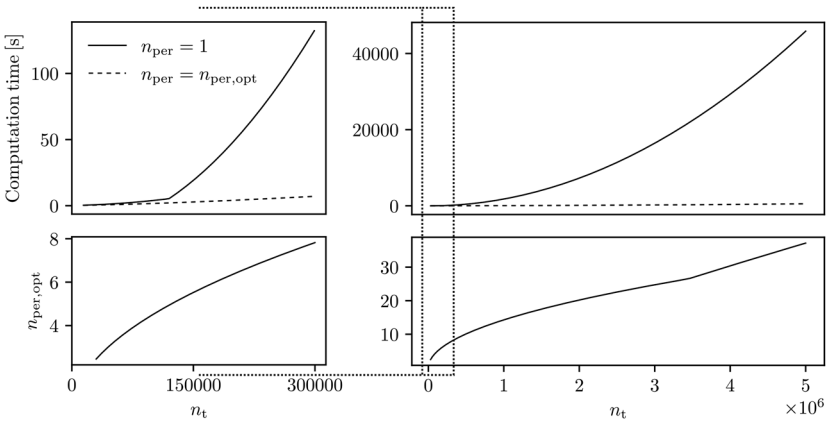

FIGURE 14 Computational time of the ground model according to Equation (24) for one period and the optimal number of periods according to Equation (25) over the total number of timesteps (top); optimal number of periods over the total number of timesteps (bottom)

leading to the total computational time for the ground model:

$$\Delta t_t = \frac{1}{2}\left(n_{per}\psi_{sa}\left(\frac{n_t}{n_{per}}^2 + \frac{n_t}{n_{per}}\right) + \frac{n_t}{n_{per}}c_{sa} + \psi_{FFT}\frac{n_t}{n_{per}}\left(n_{per}^2 + n_{per} - 2\right)\right). \tag{24}$$

To find the optimal number of periods depending on the overall number of steps Equation (24) can be minimized (derivation in Appendix A), leading to

$$n_{per} = \frac{\sqrt{\psi_{sa} n_t + c_{sa} - 2\psi_{FFT}}}{\sqrt{\psi_{FFT}}}. \tag{25}$$

If the number of steps per period n_{sp} is bigger than the n_{bp}, Equation (25) has to be solved iteratively incorporating Equations (20) and (21). Figure 14 shows the computational time of the ground model according to Equations (24) and (20)–(21) with the optimal number of periods according to Equation (25) and just one period. While the model expects integer period numbers, Equation (25) also returns floating point numbers, which have to be rounded accordingly. Depending on the total number of steps the reduction is several orders of magnitude. A value of timesteps equal to approx. 3.4×10^6 represents the break point up to which the equations can be solved with $\psi_{sa}^{<}$ and $c_{sa}^{<}$.

3 | RESULTS

3.1 | Verification of the borehole models

To validate the modelling approach, we compare our results to those obtained using the finite element software FEFLOW. The TRCMs used here are also implemented in FEFLOW by default, so that the same implementation can be compared. The boundary conditions are inspired by Diersch et al.[39] and have no physical relevance. Nevertheless, they are suitable to confirm the correct implementation. For the borehole models, the temperature at the borehole wall is set to a constant

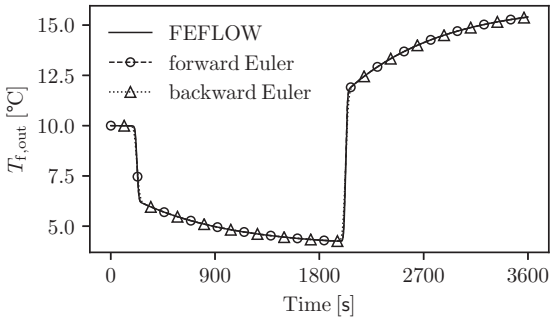

FIGURE 15 Comparison between the presented model and FEFLOW for a 1U-BHE

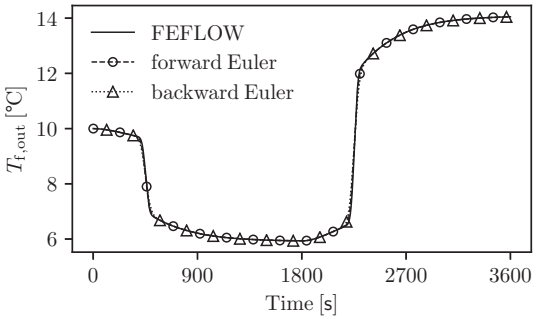

FIGURE 16 Comparison between the presented model and FEFLOW for a 2U-BHE

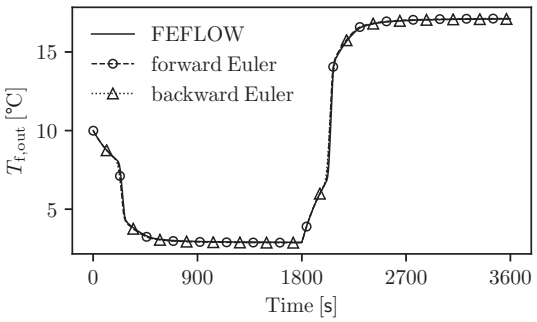

FIGURE 17 Comparison between the presented model and FEFLOW for a Coax-BHE

value of 10°C. The inlet temperature is set to 0°C for the first 1800 s and then switched to 20°C for another 1800 s. The time period of 1800 s was chosen because a steady state is reached relatively quickly due to the constant borehole wall temperature. The temperatures are chosen arbitrarily within the range of a real operation as the validation of equations and methodology is independent of the chosen temperatures. The same applies to any other parameters with the exception of the flow rate, which is why they are not shown here. Depending on the Reynolds number, different equations[27,39] are used for the Nusselt numbers, which are used to calculate the convective resistances, for a laminar, turbulent or transition flow. In the examples shown here, the flow rate was set to $41\mathrm{m}^3\mathrm{d}^{-1}$, leading to flow in the transition region for all pipes except for the outlet pipe of the Coax-BHE where the flow is turbulent due to the geometry and cross-sectional area. We have checked the implementation for other flow conditions with equally satisfying results. Figures 15–17 show the results for all three BHE models. Both the forward and backward Euler implementations show a very good agreement with the FEFLOW simulations.

TABLE 1 BHE and ground properties of the BHE field

Parameter	Value	Units
Fuild properties		
Thermal conductivity	0.43	$W\,m^{-1}K^{-1}$
Density	1054	$kg\,m^{-3}$
Volumetric heat capacity	3800000	$J\,m^{-3}K^{-1}$
Dynamic viscosity	0.0035	Pa s
BHE geometry		
Length	100	m
Diameter	0.152	m
Shank space	0.04	m
Outer diameter pipes	0.032	m
Pipe wall thickness	0.0029	m
BHE-properties		
Thermal conductivity grout	2.0	$W\,m^{-1}K^{-1}$
Volumetric heat capacity grout	1000,000	$J\,m^{-3}K^{-1}$
Thermal conductivity pipe	0.3	$W\,m^{-1}\,K^{-1}$
Ground properties		
Average thermal conductivity	2.3	$W\,m^{-1}K^{-1}$
Average volumetric heat capacity	2300,000	$J\,m^{-1}\,K^{-1}$
Undisturbed ground temperature	12.0[a]	°C

[a]Increased from 10.7°C to 12°C to account for the predominant cooling operation of the past 6 years of operation.

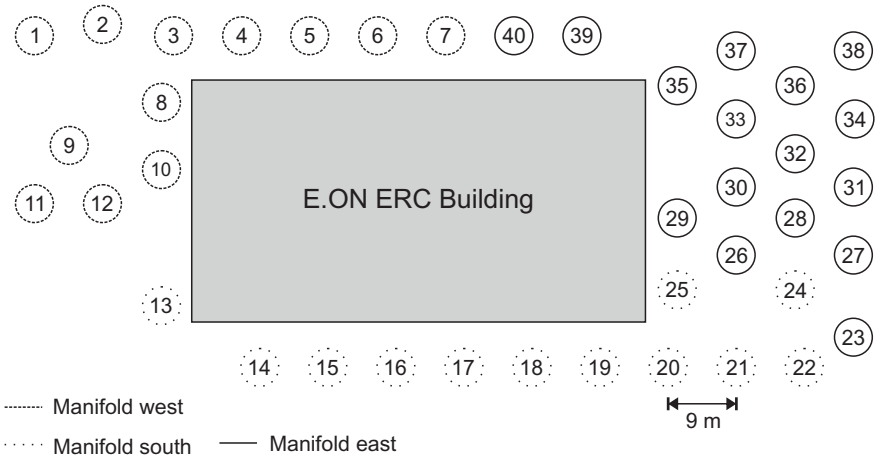

FIGURE 18 Schematic representation of the BHE arrangement at E.ON ERC building

3.2 | Comparison with monitored field data

This section shows a comparison with a real bore field consisting of 40 2U-BHEs that provides heating and cooling energy for the office building of the E.ON Energy Research Centre (E.ON ERC) at RWTH Aachen University. The entire supply system of the building is monitored in the framework of a research project of the E.ON ERC. In addition to the monitoring data, there is a high-quality ground model, which was created using outcrops, logging measurements, enhanced thermal response tests and measurements with temperature sensor modules. A detailed description of the bore field and related parameters can be found in Clauser et al.[43] The ground consists of various soil types with varying thermal properties. For the calculations here, however, the smeared properties obtained from a thermal response test were used as listed in Table 1 together with all other parameters.

Fluid inlet and outlet temperatures as well as flow rate were recorded for each borehole individually at an interval of 30 s from July 2018 to June 2019. The BHE field is divided into three manifolds (Figure 18). The manifolds are connected in parallel to the heat pump. Within the manifolds, the associated BHEs are then connected in parallel with the same

TABLE 2 Computational time per timestep for different discretizations

$\dot{V}$	BHE model	n_c [-]	Δt [s]	Comp. time per step [1×10^{-5}s]	Comp. time for $\Delta t = 30$s [1×10^{-5}s]
Const.	Forward	5	30	4.4	4.4
	Backward	5	1.5 / 30	6.6	6.6
	Forward	100	1.5	4.7	$20 \cdot 4.7 = 94$
	Backward	100	1.5 / 30	24.7	24.7
Variable	Forward	5	30	4.8	4.8
	Backward	5	1.5 / 30	24.5	24.5
	Forward	100	1.5	5.2	$20 \cdot 5.2 = 104$
	Backward	100	1.5 / 30	244	244

flow rate and inlet temperature. The measuring units are installed in the manifolds. The horizontal supply pipes between the manifolds and the top of the BHEs are up to 60-m long. Any heat losses or heat gains along these supply pipes are not considered in our model. This simplification still allows obtaining satisfactory results against the measured data and does not detract from the objective of showing the efficiency of our proposed algorithm. A first comparison is made with a single BHE, and then for the entire BHE field. However, the large distances between the BHEs and the thermal properties of the ground prevent any significant thermal interactions between the BHEs for the investigated periods.

3.2.1 | Modelling of a single BHE

BHE 18 was chosen for the single BHE comparison, as the length of the supply pipe between the BHE head and the measuring point is only 3 m. Multiple scenarios are to be investigated with respect to computational time and accuracy. These include a coarse and a fine vertical discretization as well as simulations with constant and time-variable flow rates. The simulations are carried out with both the forward and backward Euler borehole models. The maximum measured flow rate of the fluid in the entire field is $52.4\text{m}^{-1}\text{d}^{-1}$. Applying Equation (5) to this flow rate and the BHE properties in Table 1 leads to a minimum cell height of 18.51m for the recorded 30 s timestep or to a maximum timestep of 1.77 s if the cell height is set to 1 m. For the 30-s timestep we choose five cells with a height of 20 m. Both cases are considered below as examples of a coarse and a fine vertical discretization. The chosen timestep for the fine discretization is 1.5 s, leading to 20 timesteps for each measured timestep of 30 s.

Table 2 shows the computational time of the borehole models. These are the times required by the BHE models to calculate the new temperatures within the BHE. Further steps, such as reading the ground temperature and setting it as a boundary condition at the borehole wall, are not considered as they are independent of the Euler scheme or discretization. The computational times per timestep are independent of the timestep size Δt. Looking at scenarios with constant flow rates, the forward implementation is faster for both cases and rather independent of the vertical discretization. However, if the goal is to simulate a BHE with 100 cells, which corresponds to a vertical cell height of 1 m for this case and a timestep of $\Delta t = 30$s and a constant flow rate, the backward implementation is faster as 20 timesteps with the forward model would correspond to one timestep with the backward model ($20 \cdot 4.7 = 94 < 1 \cdot 24.7$, note that the computational time for $\Delta t = 30$s equal to the computational time for $\Delta t = 1.5$s). For the scenarios with time-variable flow rates, the forward implementation is superior in terms of computational time for both discretizations. Unlike the backward model, where the entire BHE matrix needs to be rebuilt, only the flow rate dependent coefficients have to be recalculated. Even for the fine discretization, it would be twice as fast to compute 20 timesteps at 1.5 s with the forward model compared to one 30-s timestep with the backward model. The vertical discretization must be chosen according to the stability criterion as a function of the maximum flow rate. For any lower flow rates, the numerical diffusion increases due to the chosen upwind scheme, which may result in decreasing accuracy.

July 2018 was chosen for the first simulation, containing 89,280 values of each measured quantity. Applying Equation (25) leads to an optimal number of 5.8 periods for this simulation. To verify the presented hybrid approach and Equation (25), multiple simulations with different number of periods as listed in Table 3 are carried out. The minimum measured calculation time is at 6 periods as projected, although the variations between all simulations are rather small.

Figure 19 shows the observed total computational times as listed in Table 3 compared to the calculated computational times using Equation (24). The curves have the same shape with an offset of around 13 s between both values. An offset

TABLE 3 Computational time for varying periods (forward model, $n_c = 5$, $\Delta t = 30$ s, $\dot{V}$ = const.)

n_{per}	n_{sp}	Comp. time [s]
1	89,280	15.05
2	44,640	14.03
4	22,320	13.52
5	17,856	13.27
6	14,880	13.05
10	8928	13.26
20	4464	13.74
30	2976	14.40
40	2232	15.31

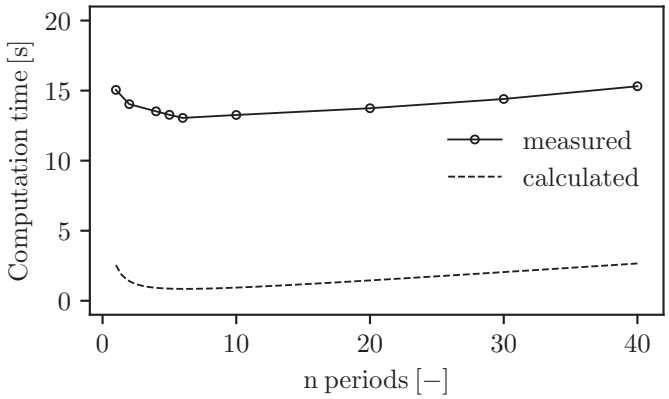

FIGURE 19 Measured total computational time and calculated computational time for the ground model for a simulation period with 89,280 steps

TABLE 4 Computational time per timestep for different discretizations

$\dot{V}$	BHE model	n_c [-]	Δt [s]	Comp. time [s]	MAE [K]
Const.	Forward	5	30	13.3	0.049
	Backward	5	30	17.5	0.044
	Forward	100	1.5	217.2	0.042
	Backward	100	30	51.6	0.039
Variable	Forward	5	30	13.8	0.049
	Backward	5	30	37.1	0.044
	Forward	100	1.5	222.6	0.042
	Backward	100	30	276.2	0.039

is expected as the calculated computational time neglects the computational time for the BHE model and any framework around the models, e.g. caching the initial state of the BHE model, setting the boundary conditions or calculating the ground load increments. Critically, the comparison shows that the chosen approach predicts the relative computational time improvements for different periods correctly. For the given example, the computational time can be reduced by 13% by increasing n_{per} from 1 to 6. With further increasing n_{per}, the computational time increases rather slowly as indicated by Equation (24).

Based on these results, all of the following models are simulated with six periods. Table 4 summarizes the results in terms of computational time and accuracy. The use of a constant flow rate averaged over time has no effect on the accuracy for the period investigated. This was to be expected, as the flow rate fluctuates only slightly around a constant value (Figure 20, middle).

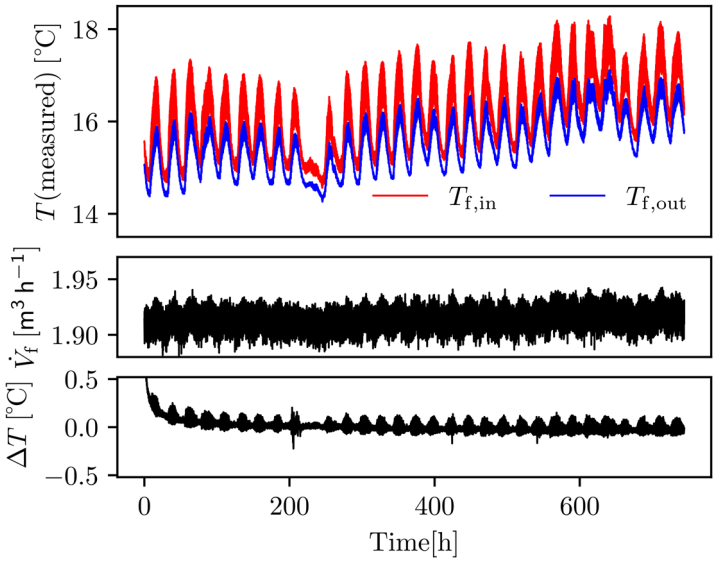

FIGURE 20 Measured fluid temperatures (top), flow rate (middle) and difference between measured and simulated outlet temperatures (bottom) for the 1-month simulation

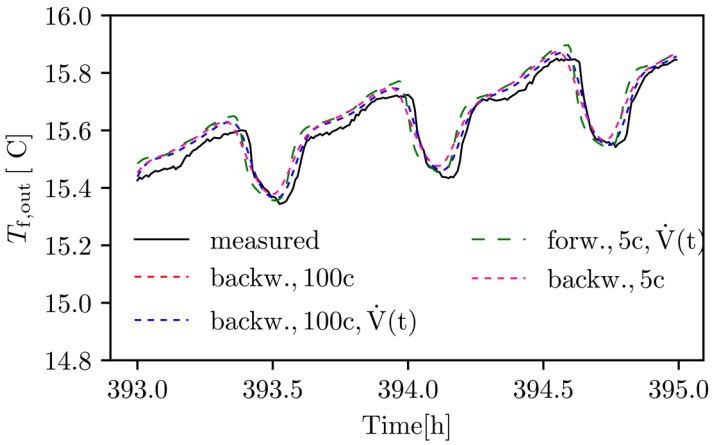

FIGURE 21 Two-hour segment of the 1-month simulation. Comparison of the measured and simulated outlet temperatures

Figure 20 shows the results for backward model with 100 cells and a time variable flow rate. While the top and middle part of Figure 20 show the measured values, the bottom part shows the difference between the measured and simulated outlet temperatures. The figure shows that the difference is decreasing within the first 100 h. The deviation at the start of the simulation is due to the thermal impact of the past operation of the BHE, which was not considered in the simulation. Figure 21 shows a 2-h period extracted from Figure 20. The influence of the time variable flow rate is so small that the curves for the 100 cell backward model overlap and are indistinguishable. The deviations between measurement and simulation are caused by three components shown in Figure 22. All models have a slight offset in the simulated return temperatures (e_1). Furthermore, all models have a slight offset along the time axis (e_2). The third type of error e_3 is a smeared reaction to rapidly changing fluid inlet temperatures. In Figure 22, this can be seen clearly for the backward model. This error is caused by the numerical diffusion due to the upwind scheme and can be reduced with finer discretizations for the backward model. For the forward model, it can be completely eliminated by forcing the CFL number to 1. However, a CFL number of 1 does not necessarily lead to the most accurate result, as the model does not consider natural diffusion that occurs in reality. For the forward model in Figure 22, the CFL number is approximately 0.6, which coincidentally matches the slope of the measured curve quite well. While error types e_1 and e_2 are rather independent of the BHE model type and discretization, error type e_3 can be influenced accordingly. Figure 22 also shows the problems that arise when using the mean absolute error (MAE). Although the forward model generally represents the characteristic of the curve better, the deviations for the backward model are smaller overall due to smearing. The MAEs are, therefore, only given to show that the models basically work; they are unsuitable for comparing the models with each other without further consideration, which is not the focus of this paper.

Next, the simulation period is extended to a full year consisting of 1051, 200 timesteps at 30 s. Applying Equation (25) results in an optimal number of 19.7 periods for this simulation. To incorporate the small influence of the variable flow

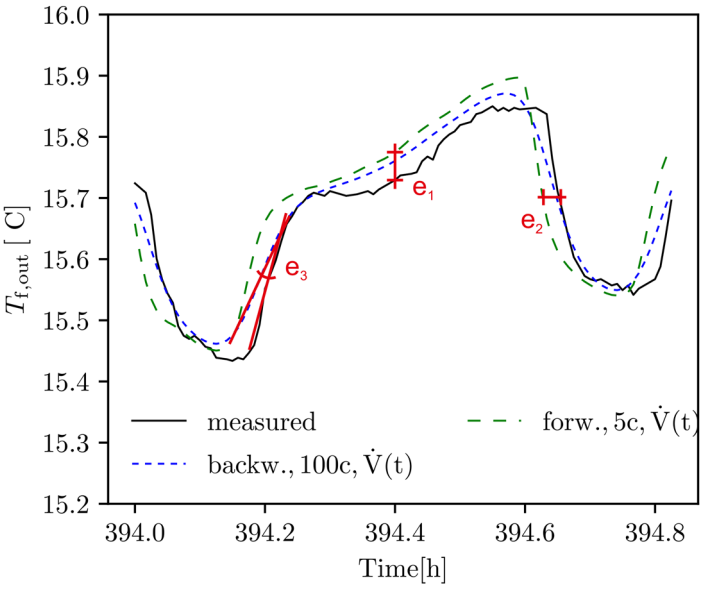

FIGURE 22 Different types of deviation between measured and simulated outlet temperatures

TABLE 5 Computational time for varying periods (forward model, $n_c = 5$, $\Delta t = 30$ s)

n_{per}	n_{sp}	Comp. time [s]
1	1051,200	1726.6
5	210,240	350.2
10	105,120	183.3
16	65,700	172.2
18	58,400	174.6
20	52,560	175.5
30	35,040	176.2
40	26,280	180.1
80	13,140	202.3
120	8760	231.9
240	4380	312.0

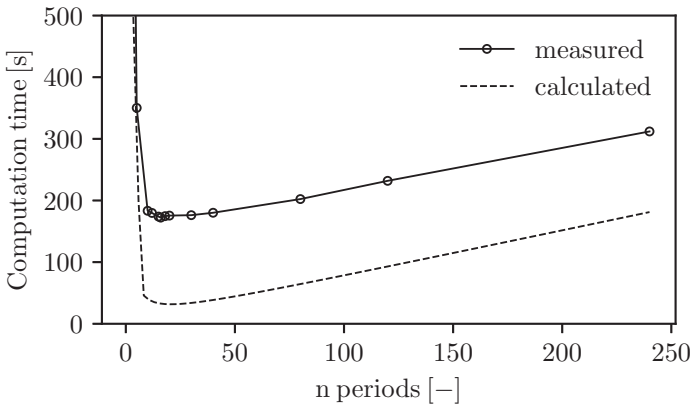

FIGURE 23 Measured total computational time and calculated computational time for the ground model for a simulation period with 1051,200 steps

rate, the flow rate in the following simulations is only adjusted if it changes by more than ±5% between different consecutive timesteps. All simulations are performed with the five cell forward model, leading to a MAE of 0.032K. Table 5 and Figure 23 show the results for different n_{per}. In this case, the calculated optimum of $n_{per} = 19.7$ does not lead to the lowest computational time, which is at 16. Although the calculated optimum is four periods off, the computational times in this range differ only slightly. By increasing the number of periods from 1 to 16, the computational time could be reduced by

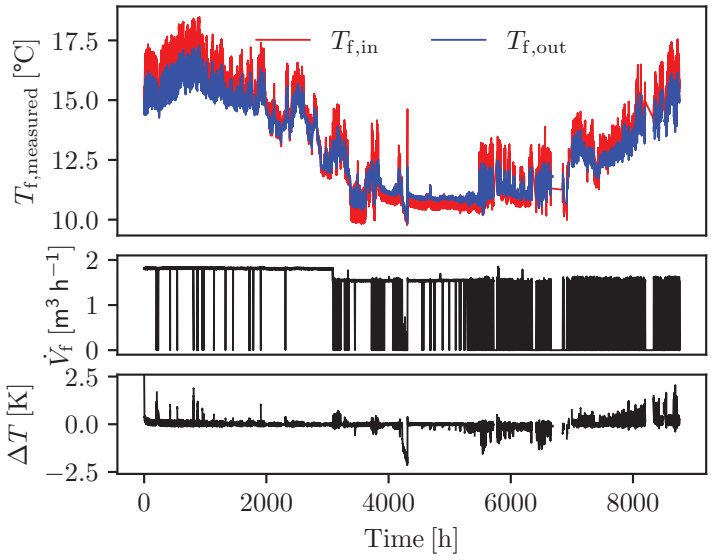

FIGURE 24 Measured fluid temperatures (top), flow rate (middle) and difference between measured and simulated outlet temperatures (bottom) for the 1-year simulation

90% while the difference between $n_{per} = 20$ and $n_{per} = 16$ in relation to $n_{per} = 1$ is less than 1%. It shows nevertheless that Equation (25) is only an approximation.

Figure 24 shows the results analogue to Figure 20 for the 1-year simulation. The increasing deviation between calculated and measured outlet temperatures towards the end of the simulation period is related to the short cycle times of the circulation pump, which are sometimes less than 30 m. Every time the circulation pump is switched on again, there are briefly larger deviations due to the fluid stagnating in the supply line, which is not considered in the simulation.

3.2.2 | Modelling the whole field

For the simulation of multiple BHEs, the effort of the ground simulation increases theoretically quadratically to the number of boreholes, as the temperature change for each borehole has to be calculated not just for the borehole itself but for the rest. For further reduction of the computational time, the calculation of the FFT model for the simulation of multiple BHEs is parallelised. Accordingly, the time reduction potential when using the hybrid model should be even greater than for the single BHE. To illustrate this, all 40 BHE are simulated as one bore field over a simulation period of one year corresponding to 1051, 200 timesteps of 30 s. With consideration of the parallelisation, ψ_{FFT} was redetermined to 7.8×10^{-4}, which is one order of magnitude smaller than $1.58 \times 10^{-6} \cdot 40^2 = 2.53 \times 10^{-3}$. To check for possible scaling effects in the semi-analytical model, its parameters were also redetermined for the simulation of 40 BHE, leading to

$$\psi_{sa} = \begin{cases} 1.9 \times 10^{-6} & \text{for } n_r < 130,000 \\ 5.3 \times 10^{-6} & \text{for } n_r \geq 130,000 \end{cases} \tag{26}$$

and

$$c_{sa} = \begin{cases} 3.4 \times 10^{-3} & \text{for } n_r < 130,000 \\ -5.5 \times 10^{-2} & \text{for } n_r \geq 130,000 \end{cases} \tag{27}$$

The newly determined values are partly above, below or in the range of the old values multiplied by 40^2, indicating some scaling effects, and showing the uncertainties associated with the measurement of the computational times. Applying Equation (25) with these parameters leads to an optimal number of 50.6 periods.

The computational times for different numbers of periods are listed in Table 6 and displayed in Figure 25. By increasing the number of periods from 1 to 50, the computational time could be reduced by 98.4%. In this case, the optimal number of periods coincides with the measured computational times. Figure 26 shows the MAE for all BHE for the full year simulation. Some of the BHEs have only been in operation towards the end of the investigated period when the short cycle times of the heat pump started or had measurement problems. These BHEs are displayed as empty circles. Excluding

TABLE 6 Computational time for varying periods for all 40 BHE (forward model, $n_c = 5$, $\Delta t = 30$) s

n_{per}	n_{sp}	Comp. time [h]
1	1051,200	873.1
10	105,120	40.3
20	52,560	22.3
30	35,040	17.8
40	26,280	16.6
50	21,024	14.1
60	17,520	16.2
80	13,140	17.1

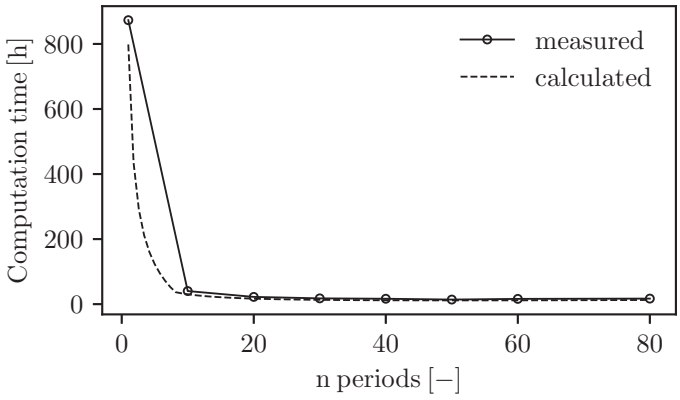

FIGURE 25 Measured total computational time and calculated computational time for the ground model for a simulation period with 1051,200 steps and 40 BHE

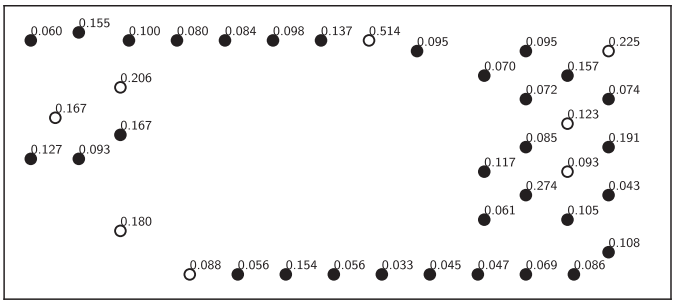

FIGURE 26 BHE layout with MAE for the 1-year simulation. BHEs with measurement problems as empty circles

these, the MAE of all BHEs is within the accuracy of the sensors, which is ±0.1 K for both inlet and outlet temperatures in the given temperature range.

4 | DISCUSSION AND CONCLUSIONS

By extending a semi-analytical simulation model for BHE with the FFT approach, the computational time of the model could be reduced significantly. As the reduction occurs in the simulation of the ground, the extent depends on the share of the ground simulation in the total simulation. Furthermore, it was shown that the computational efficiency becomes especially significant for high numbers of timesteps, since the calculation time of the original model grows exponentially with the number of timesteps. While the time reduction for a simulation of a single BHE with 89, 280 timesteps was only 13%, the reduction for a simulation with 1051200 timesteps increased to 90%. When simulating the entire field with 40 BHEs, the reduction was in fact 98%. By integrating the FFT into the model, real operating periods of several years can now be simulated efficiently with high temporal resolution without the use of a load aggregation scheme. This can be particularly interesting for cases where the BHE simulation is coupled with other models that require high temporal resolutions. A simple equation based on measured computational times of the model was derived for the determination of the optimal number of periods depending on the total number of timesteps of a simulation period. Increasing the

number of periods initially leads to a considerable improvement up to this optimal. After reaching the optimal number of periods, the computational time increases only moderately with further increasing number of periods. It is, therefore, rather advisable to round up the number of selected periods. The simplified assumption of a linear relation between timesteps and computational time for the ground models can introduce a mismatch between the projected optimal number of periods and the actual number of periods with the lowest computational time in some cases. However, the deviations are negligible compared to the improvement achieved by the hybrid approach.

Furthermore, the forward and backward Euler implementations were compared for different use cases. Depending on the use case, one or the other model is superior with respect to computational time as summarised below:

- The forward Euler model has a much lower computational time per timestep and is comparatively independent of the spatial discretization.
- Depending on the discretization, time-variable flow rates lead to a multiplication of the computing time for the backward Euler model.
- The forward Euler model must be discretized according to the CFL criteria for the maximum volume flow rate for time-variable flow rates. For all smaller flow rates the numerical diffusion increases, which can lead to a accuracy reduction.
- The backward model is advantageous for larger timesteps or high flow rates.

By implementing and publishing the model in Python, easy adaptation and further development are possible. In future work, the model will be coupled with other system models such as heat pumps or solar collectors.

ACKNOWLEDGMENT

Open access funding enabled and organized by Projekt DEAL.

DATA AVAILABILITY STATEMENT

The data that support the findings of this study are openly available in *Hybrid-BHE-Simulation-Model* at https://github.com/GUT-Aachen, https://doi.org/10.5281/zenodo.5971257.

ORCID


Stephan Düber https://orcid.org/0000-0001-7029-7303

REFERENCES

1. Spitler J, Bernier M. 2 – Vertical borehole ground heat exchanger design methods. In: Rees SJ, ed. *Advances in Ground-Source Heat Pump Systems*. Woodhead Publishing; 2016:29-61.
2. Eskilson P. *Thermal Analysis of Heat Extraction Boreholes*. Ph. D. thesis. University of Lund; 1987.
3. Carslaw HS, Jaeger JC. *Conduction of Heat in Solids*. Oxford University; 1959.
4. Marcotte D, Pasquier P. Fast fluid and ground temperature computation for geothermal ground-loop heat exchanger systems. *Geothermics*. 2008;37(6):651-665.
5. Yavuzturk C, Spitler JD, Rees SJ, et al. A transient two-dimensional finite volume model for the simulation of vertical U-tube ground heat exchangers. *ASHRAE Trans*. 1999;105(2):465-474.
6. Ingersoll LR. Theory of the ground pipe heat source for the heat pump. In: *Heating Piping and Air Conditioning*. Domestic Engineering Co. Vol. 20. 1948:119-122.
7. Zeng HY, Diao NR, Fang ZH. A finite line-source model for boreholes in geothermal heat exchangers. *Heat Transfer-Asian Research: Co-sponsored by the Society of Chemical Engineers of Japan and the Heat Transfer Division of ASME*. 2002;31(72):558-567.
8. Ingersoll L, Zobel O, Ingersoll A. *Heat Conduction: With Engineering, Geological, and Other Applications*. McGraw-Hill; 1954.
9. Bernier MA. Ground-coupled heat pump system simulation/discussion. *ASHRAE Trans*. 2001;107:605-616.
10. Man Y, Yang H, Diao N, Liu J, Fang Z. A new model and analytical solutions for borehole and pile ground heat exchangers. *Int J Heat Mass Transfer*. 2010;53(13-14):2593-2601.
11. Philippe M, Bernier M, Marchio D. Validity ranges of three analytical solutions to heat transfer in the vicinity of single boreholes. *Geothermics*. 2009;38(4):407-413.
12. Li M, Li P, Chan V, Lai AC. Full-scale temperature response function (G-function) for heat transfer by borehole ground heat exchangers (GHEs) from sub-hour to decades. *Appl Energy*. 2014;136:197-205. doi:10.1016/j.apenergy.2014.09.013
13. Sutton MG, Nutter DW, Couvillion RJ. A ground resistance for vertical bore heat exchangers with groundwater flow. *J Energy Resour Technol*. 2003;125(3):183-189.

14. Molina-Giraldo N, Blum P, Zhu K, Bayer P, Fang Z. A moving finite line source model to simulate borehole heat exchangers with groundwater advection. *Int J Therm Sci*. 2011;50(12):2506-2513.
15. Zhang W, Yang H, Lu L, Fang Z. The analysis on solid cylindrical heat source model of foundation pile ground heat exchangers with groundwater flow. *Energy*. 2013;55:417-425. doi:10.1016/j.energy.2013.03.092
16. Abdelaziz SL, Ozudogru TY, Olgun CG, Martin JR. Multilayer finite line source model for vertical heat exchangers. *Geothermics*. 2014;51:406-416. doi:10.1016/j.geothermics.2014.03.004
17. Erol S, François B. Multilayer analytical model for vertical ground heat exchanger with groundwater flow. *Geothermics*. 2018;71:294-305. doi:10.1016/j.geothermics.2017.09.008
18. Cimmino M, Bernier M. A semi-analytical method to generate g-functions for geothermal bore fields. *Int J Heat Mass Transfer*. 2014;70:641-650.
19. Cimmino M. The effects of borehole thermal resistances and fluid flow rate on the g-functions of geothermal bore fields. *Int J Heat Mass Transfer*. 2015;91:1119-1127. doi:10.1016/j.ijheatmasstransfer.2015.08.041
20. Yavuzturk C, Spitler JD. A short time step response factor model for vertical ground loop heat exchangers. *ASHRAE Trans*. 1999;105(2):475-485.
21. Claesson J, Javed S. An analytical method to calculate borehole fluid temperatures for time-scales from minutes to decades. *ASHRAE Trans*. 2011;117:279-288.
22. Pasquier P, Zarrella A, Labib R. Application of artificial neural networks to near-instant construction of short-term g-functions. *Appl Therm Eng*. 2018;143:910-921. doi:10.1016/j.applthermaleng.2018.07.137
23. Loveridge F, Powrie W. Temperature response functions (G-functions) for single pile heat exchangers. *Energy*. 2013;57:554-564. doi:10.1016/j.energy.2013.04.060
24. Hellström G. *Ground Heat Storage: Thermal Analyses of Duct Storage Systems*. PhD thesis. Lund University; 1991.
25. Gu Y, O'Neal D. Development of an equivalent diameter expression for vertical U-tubes used in ground-coupled heat pumps. *ASHRAE Trans*. 1998;104:347-355.
26. Sharqawy MH, Mokheimer EM, Badr HM. Effective pipe-to-borehole thermal resistance for vertical ground heat exchangers. *Geothermics*. 2009;38(2):271-277. doi:10.1016/j.geothermics.2009.02.001
27. Bauer D, Heidemann W, Müller-Steinhagen H, Diersch HJ. Thermal resistance and capacity models for borehole heat exchangers. *Int J Energy Res*. 2011;35(4):312-320.
28. Zarrella A, Scarpa M, De Carli M. Short time step analysis of vertical ground-coupled heat exchangers: The approach of CaRM. *Renew Energy*. 2011;36(9):2357-2367.
29. Pasquier P, Marcotte D. Short-term simulation of ground heat exchanger with an improved TRCM. *Renew Energy*. 2012;46:92-99.
30. Liao Q, Zhou C, Cui W, Jen T. New correlations for thermal resistances of vertical single U-Tube ground heat exchanger. *J Therm Sci Eng Appl*. 2012;4(3):031010.
31. Eskilson P, Claesson J. Simulation model for thermally interacting heat extraction boreholes. *Numer Heat Transf*. 1988;13(2):149-165.
32. Kavanaugh SP. *Simulation and Experimental Verification of Vertical Ground-coupled Heat Pump Systems*. PhD thesis. Oklahoma State University; 1985:74078.
33. Al-Khoury R, Bonnier P. Efficient finite element formulation for geothermal heating systems. Part II: transient. *Int J Numer Methods Eng*. 2006;67(5):725-745.
34. Huber A. *Erdwärmesonden für Direktheizung. Phase 1: Modellbildung und Simulation*. Schlussbericht. Bundesamt für Energie (BFE); 2005.
35. Ruiz-Calvo F, Rosa MD, Monzó P, Montagud C, Corberán JM. Coupling short-term (B2G model) and long-term (g-function) models for ground source heat exchanger simulation in TRNSYS. Application in a real installation. *Appl Therm Eng*. 2016;102:720-732. doi:10.1016/j.applthermaleng.2016.03.127
36. Düber S. Semi-analytisches werkzeug zur dimensionierung von erdwärmesonden. In: 35. Baugrundtagung, Forum für junge Geotechnik-Ingenieure, Stuttgart, Germany, 26-28 September 2018. DGGT; 2018:211-220. Beiträge der Spezialsitzung
37. Laferrière A, Cimmino M, Picard D, Helsen L. Development and validation of a full-time-scale semi-analytical model for the short-and long-term simulation of vertical geothermal bore fields. *Geothermics*. 2020;86:101788.
38. Düber S. Hybrid simulation model for borehole heat exchangers. Version 1.0.0. https://github.com/GUT-Aachen/Hybrid-BHE-Simulation-Model
39. Diersch H, Bauer D, Heidemann W, Rühaak W, Schätzl P. Finite element formulation for borehole heat exchangers in modeling geothermal heating systems by FEFLOW. *WASY Software FEFLOW White Paper*. 2010;5:5-96.
40. Virtanen P, Gommers R, Oliphant TE, et al. SciPy 1.0: Fundamental algorithms for scientific computing in python. *Nat Methods*. 2020;17:261-272. doi:10.1038/s41592-019-0686-2
41. Treeck vCA, Frisch J, Weck-Ponten S, et al. *GeTIS - Geothermisches Informationssystem zur Bemessung, Modellierung, Bewertung und Genehmigung vernetzter geothermischer Energiesysteme auf Gebäude- und Stadtquartiersebene: Schlussbericht: Laufzeit des Vorhabens: 01.01.2016 bis 31.12.2019*. Technical report 03ET1357A. RWTH Aachen University; 2020
42. Lazzarotto A. *Developments in Ground Heat Storage Modeling*. PhD thesis. KTH Royal Institute of Technology; 2015.
43. Clauser C, Michalski A, Müller D, Fütterer J, Stinner F. *Exergetisch optimierte Betriebsführung der Wärme- und Kälteversorgung eines Gebäudes unter Nutzung eines dynamischen Regelungssystems und flexibler Einbindung eines vollständig überwachten Erdwärmesondenfeldes: Endbericht*. Technical report. Institute for Energy Efficient Buildings and Indoor Climate; 2017.

How to cite this article: Düber S, Ziegler M, Fuentes R. Development and validation of a computationally efficient hybrid model for temporal high-resolution simulations of geothermal bore fields. *Int J Numer Anal Methods*. 2022;1-22. https://doi.org/10.1002/nag.3427

APPENDIX A: DETERMINATION OF THE OPTIMAL NUMBER OF PERIODS

$$\frac{\partial}{\partial n_{\mathrm{per}}}\left(\frac{1}{2}\left(n_{\mathrm{per}}\psi_{\mathrm{sa}}\left(\frac{n_{\mathrm{t}}}{n_{\mathrm{per}}}^{2}+\frac{n_{\mathrm{t}}}{n_{\mathrm{per}}}\right)+\frac{n_{\mathrm{t}}}{n_{\mathrm{per}}}c_{\mathrm{sa}}+\psi_{\mathrm{FFT}}\frac{n_{\mathrm{t}}}{n_{\mathrm{per}}}\left(n_{\mathrm{per}}{}^{2}+n_{\mathrm{per}}-2\right)\right)\right)$$

$$=\frac{n_{\mathrm{t}}}{n_{\mathrm{per}}^{2}}\left(-0.5\psi_{\mathrm{sa}}n_{\mathrm{t}}-0.5c_{\mathrm{sa}}+\psi_{\mathrm{FFT}}\left(0.5n_{\mathrm{per}}^{2}+1\right)\right) \tag{A1}$$

$$\frac{n_{\mathrm{t}}}{n_{\mathrm{per}}^{2}}\left(-0.5\psi_{\mathrm{sa}}n_{\mathrm{t}}-0.5c_{\mathrm{sa}}+\psi_{\mathrm{FFT}}\left(0.5n_{\mathrm{per}}^{2}+1\right)\right)=0 \tag{A2}$$

$$n_{\mathrm{per}}=\pm\frac{\sqrt{\psi_{\mathrm{sa}}n_{\mathrm{t}}+c_{\mathrm{sa}}-2\psi_{\mathrm{FFT}}}}{\sqrt{\psi_{\mathrm{FFT}}}} \tag{A3}$$

APPENDIX B: DETERMINATION OF THE WEIGHTED PARAMETERS

$$\Delta t(\psi_{\mathrm{sa}})=\sum_{i=0}^{n_{\mathrm{sp}-1}}\psi_{\mathrm{sa}}(n_{\mathrm{sp}}-i)=\sum_{i=1}^{n_{\mathrm{sp}}}\psi_{\mathrm{sa}}i \tag{B4}$$

$$\Delta t(\psi_{\mathrm{sa}}^{<},\psi_{\mathrm{sa}}^{>})=\sum_{i=1}^{n_{\mathrm{b}}-1}\psi_{\mathrm{sa}}^{<}i+\sum_{i=n_{\mathrm{b}}}^{n_{\mathrm{sp}}}\psi_{\mathrm{sa}}^{>}i=\frac{1}{2}\left(\psi_{\mathrm{sa}}^{<}(n_{\mathrm{bp}}^{2}-n_{\mathrm{bp}})-\psi_{\mathrm{sa}}^{>}(n_{\mathrm{bp}}^{2}-n_{\mathrm{sp}}^{2}-n_{\mathrm{b}}-n_{\mathrm{sp}})\right) \tag{B5}$$

$$\frac{\bar{\psi}_{\mathrm{sa}}}{2}(n_{\mathrm{sp}}^{2}+n_{\mathrm{sp}})=\frac{1}{2}\left(\psi_{\mathrm{sa}}^{<}(n_{\mathrm{bp}}^{2}-n_{\mathrm{bp}})-\psi_{\mathrm{sa}}^{>}(n_{\mathrm{bp}}^{2}-n_{\mathrm{sp}}^{2}-n_{\mathrm{b}}-n_{\mathrm{sp}})\right) \tag{B6}$$

$$\bar{\psi}_{\mathrm{sa}}=\frac{n_{\mathrm{bp}}^{2}(\psi_{\mathrm{sa}}^{<}-\psi_{\mathrm{sa}}^{>})+n_{\mathrm{bp}}(\psi_{\mathrm{sa}}^{>}-\psi_{\mathrm{sa}}^{<})+\psi_{\mathrm{sa}}^{>}(n_{\mathrm{sp}}^{2}+n_{\mathrm{sp}})}{n_{\mathrm{sp}}^{2}-n_{\mathrm{sp}}} \tag{B7}$$